Layer-by-layer self-assembly of MoS$_2$, rGO and polypyrrole nanotubes for enhanced electrochemical performance of supercapacitor

3.1 Introduction:

In the previous chapter, ternary nanocomposites of MoS$_2$, rGO and PEDOTNPs was discussed for supercapacitor applications and the PEDOTNPs based ternary system is found to be a promising system when stability is concerned. The motivation of working with ternary nanocomposites was explained in the Chapter 2 (section 2.1). Inspired from the previous work, another conducting polymer named polypyrrole (PPy) was explored for further studies on supercapacitor. This chapter deals with polypyrrole (PPy) based ternary nanocomposites for supercapacitor applications. Polypyrrole is a promising pseudocapacitive material with large electrochemical potential window, high storage capacity, tunable electrical conductivity and higher energy density [1, 2]. It offers specific capacitance in the range of 100-400 Fg^{-1}. The morphology of electrode materials plays a remarkable role in energy storage. 1-D polypyrrole nanotubes are ideal building blocks to fabricate nanoscale devices due to the availability of radially accessible surface area and open tubular networks [3]. Similar to the work presented in Chapter 2, layered molybdenum disulfide/reduced graphene oxide (MoS$_2$/rGO) nanocomposite was synthesized by layer-by-layer self-assembly method in order to prevent the agglomeration and effective utilization of the surface area of reduced graphene oxide (rGO) nanosheets. Ternary MoS$_2$-rGO/PPyNTs nanocomposite was obtained by combining pre-synthesized polypyrrole nanotubes (PPyNTs) with layered MoS$_2$-GO followed by *in-situ* hydrothermal reduction of GO. MoS$_2$-PPyNTs, rGO-PPyNTs and PPyNTs electrodes were also prepared and compared their electrochemical performance with the ternary electrode. The synergetic effect of layer-by-layer assembly of MoS$_2$ and rGO nanosheets with PPyNTs imparts immense electrochemical activity which is described in this chapter.

3.2 Experimental

3.2.1 Materials: Molybdenum (IV) disulphide (MoS$_2$) powder, graphite powder (< 20 μm), Iron (III) Chloride (FeCl$_3$ - 97%), pyrrole monomer (98%) were purchased from Sigma-Aldrich. Cetyltrimethyl ammonium bromide (CTAB, Hi-media), methyl

orange indicator (SRL) and Potassium permanganate (Merck Emplura) were also use in different steps of the synthesis process. The laboratory reagents Sulfuric acid (H_2SO_4) and Phosphoric acid (H_3PO_4) were obtained from avantor.

3.2.2 Exfoliation of MoS₂, Synthesis of graphene oxide (GO) nanosheets and Preparation of MoS₂-rGO structures: Liquid phase exfoliation of bulk MoS_2 and development of MoS_2-rGO layer-by-layer structures were carried out as described in the section no. 2.2.2 of the Chapter 2. Graphite oxide nanosheets were prepared from improved hummers method [4].

3.2.3 Synthesis of MoS₂-rGO/PPyNTs ternary nanocomposites: Polypyrrole nanotubes were synthesized with self-degradation template using methyl orange and ferric chlorite [5]. The prepared MoS_2-GO structures were dispersed in N-Methyl-2-pyrrolidone (NMP) using ultrasound for 20 minutes followed by addition of PPyNTs (40 wt%) and again ultrasonicated for another 2 h. Obtained black colored dispersion was transferred to a teflon coated autoclave and annealed at 200 °C for 24 h to reduce the graphene oxide. The black colored precipitate was first washed with NMP to remove organic solvent and later centrifuged with DD water and ethanol for several times. Then the product was dried in vacuum at 60 °C for 12 h. rGO-PPyNTs and MoS_2-PPyNTs binary nanocomposites were also prepared by maintaining 40 wt% ratios between PPyNTs and rGO/MoS_2.

3.2.4 Structural and morphological characterization: Powder X-ray diffraction (P-XRD) was performed in D8 focus X-ray diffractometer, Bruker AXS, Germany (make) at a scan rate of 1°/min. Zeta potential and dynamic light scattering (DLS) was measured in Malvern Zetasizer Nano series, Nano ZS90. Surface morphology was recorded in scanning electron microscope (SEM) using JEOL, JAPAN, JSM 6390LV at 20 kV accelerating voltage. Transmission Electron Microscopy (TEM) images were taken by JEM-2100 at 60-200 KV in 50V steps. Brunauer-Emmett-Teller (BET) measurements were performed by using quantachrom model instrument using nova software to determine the surface area and pore diameter.

3.2.5 Electrochemical measurements: All the electrochemical measurements were evaluated at room temperature in three electrode system (AUTOLAB 302N Modular Potentiostat Galvanostat, FRA32M Module/ Kanaalweg 29/G, 3526 KM Utrecht, Netherlands). Ag/AgCl containing 3 M KCl was employed as reference electrode, platinum as counter electrode and ITO with the active material was used as working electrode for three electrode system. The working electrodes were prepared by incorporating the active material with carbon black and nafion by maintaining a mass ratio 85:10:5. Obtained slurry was drop casted on ITO coated glasses (dimension = 1x0.5 cm^2) followed by drying at desiccator. The mass of the active material was maintained nearly 1 mg for all the prepared electrodes. 1 M KCl was used as electrolyte for the electrochemical measurements. Cyclic voltammetry (CV), galvanostatic charge-discharge (GCD) and electrochemical impedance spectroscopy (EIS) were performed to study the electrochemical performance of the nanocomposites. EIS was conducted in AUTO FRA modular in 1 M KCl solution within a frequency range 100 KHz to 20 Hz.

3.3 Results and discussion

3.3.1 Schematic representation: Schematic representation of the fabrication process of ternary MoS$_2$-rGO/PPyNTs nanocomposites is described in Scheme 3.I. After preparation of positively charged MoS$_2$ and negatively charged GO nanosheets, the colloidal suspensions were stirred together to obtain heterogeneous layer-by-layer assembly of MoS$_2$-GO. The possible direction of self-assembly of MoS$_2$ and GO are shown in MoS$_2$-GO composite in scheme 3.I. Ternary MoS$_2$-rGO/PPyNTs nanocomposite was obtained after addition of PPyNTs and hydrothermal reduction of GO.

3.3.2 Zeta potential measurements: Surface charge of exfoliated MoS$_2$ and graphene oxide nanosheets were investigated with zeta potential analyzer. The dispersion of CTAB exfoliated MoS$_2$ and graphene oxide was stable in water due to electrostatic repulsion between the nanosheets. Zeta potential analysis gives a better insight in our study. Mostly, particles with zeta potential higher than ±30 mV can form a stable dispersion due to inter-particular electrostatic repulsion [9]. Figure 3.1 displays the zeta potential measurement of both CTAB peel off MoS$_2$ and graphene
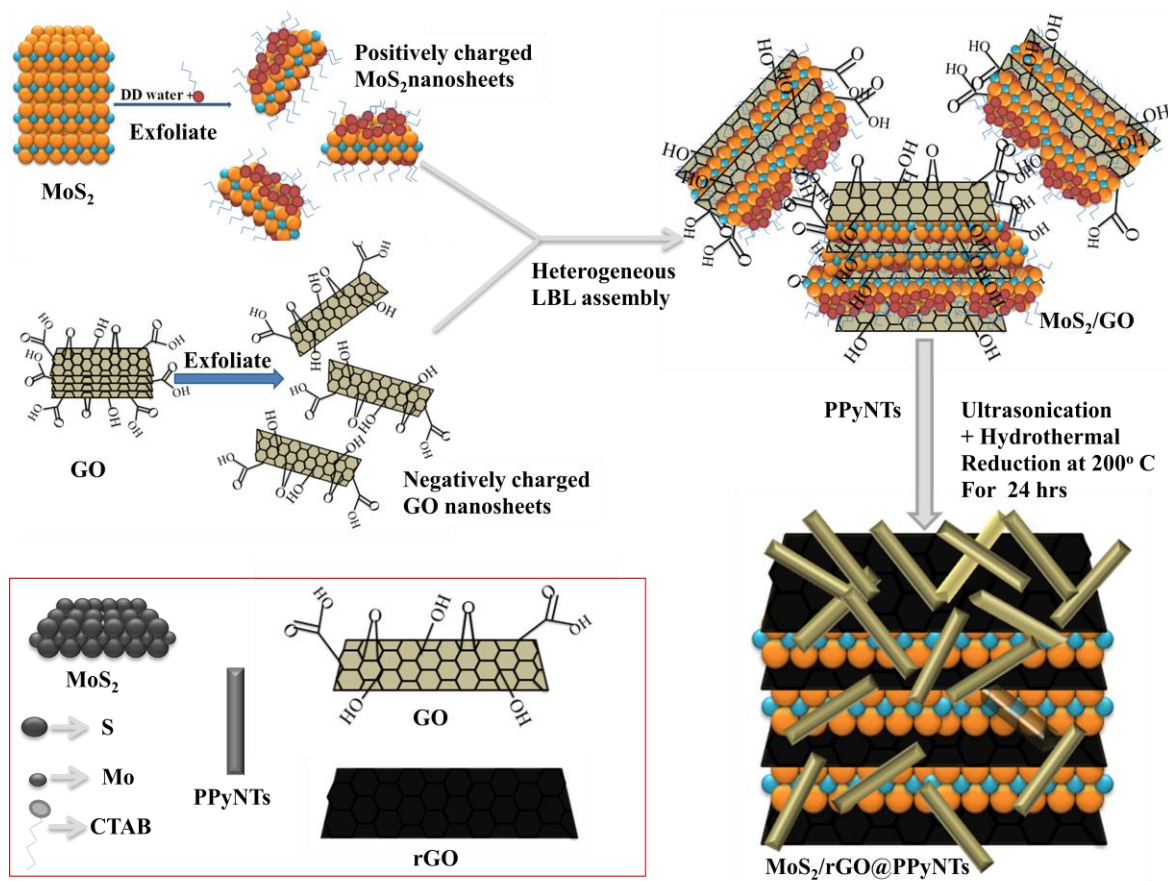
Scheme 3.I: Schematic presentation of synthesis of layer-by-layer self-assembly of MoS₂-GO and MoS₂-rGO/PPyNTs nanocomposite.
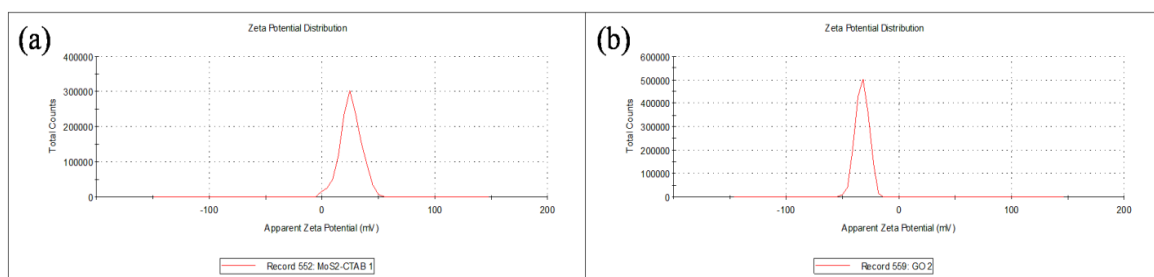

Figure 3.1: Zeta potential curves of (a) CTAB exfoliated MoS₂ and (b) graphene oxide (GO).

oxides suspension in DD water. It is interesting to note that, the zeta potential of CTAB assists MoS₂ is found to be +25.5 mV but the colloidal suspension is stable in water over months, which may be due to the similar surface energy of 1% CTAB containing water with MoS₂. GO-water suspension is quite stable with a zeta potential

of -31.1mV. We also examined the particle size of exfoliated MoS_2, graphene oxide and MoS_2-GO and the obtained average particle sizes were 121.4 nm, 298.5 nm and 480.8 nm respectively.

3.3.3 Scanning Electron Microscopy: Figure 3.2 shows the SEM images of MoS_2-GO, MoS_2-rGO and MoS_2-rGO/PPyNTs nanocomposites. SEM micrograph of MoS_2-GO composite shows some layered arrangement and the layers are nearly parallel to each other. MoS_2 nanosheets are absorbed on the GO nanosheets surface due to the opposite charge attraction between them. MoS_2-rGO (Figure 3.2 b) layer-by-layer structure is more porous when compared with MoS_2-GO (Figure 3.2 a) which may be attributed to the removal of surface functionalized oxygen groups after reduction of GO. PPyNTs envelop the MoS_2-rGO nanosheets in the ternary nanocomposite as observed from SEM images (Figure 3.2 c, d). Elemental mapping of the MoS_2-rGO/PPyNTs ternary nanocomposite (Figure 3.2 e) shows the presence of carbon, oxygen and sulfur. Here, PPyNTs cover the MoS_2-rGO layer-by-layer structures and Mo locates in between two layers of S in MoS_2. This may be reason of absence of Mo in the elemental mapping of SEM as the secondary electrons cannot penetrate deeper inside the nanocomposites.
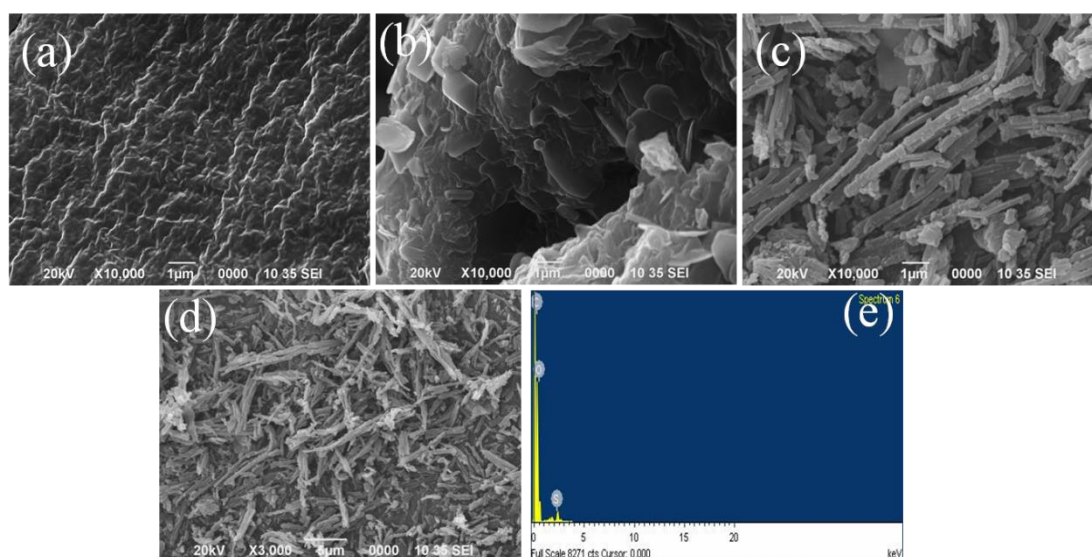
Figure 3.2: SEM micrographs of (a) MoS_2-GO, (b) MoS_2-rGO, (c) MoS_2-rGO/PPyNTs and (d) MoS_2-rGO/PPyNTs at different magnifications and (e) EDX spectrum of MoS_2-rGO/PPyNTs.

3.3.4 Transmission Electron Microscopy: TEM micrographs of MoS_2, rGO, MoS_2-rGO, PPyNTs, MoS_2-rGO/PPyNTs nanocomposites are depicted in Figure 3.3. MoS_2 nanosheets and rGO nanosheets are observed in Figure 3.3 a, b respectively. After addition of MoS_2 in rGO, the agglomeration of rGO decreases. Large nanosheets of rGO without any agglomeration could be observed from the TEM micrograph of MoS_2-rGO structure (Figure 3.3 c) and the morphology is completely different from pristine rGO nanosheets (Figure 3.3 b). Figure 3.3 (d) shows the TEM image of PPyNTs and the average diameter of the nanotubes is calculated to be nearly 170 nm. For rGO-PPyNTs nanocomposite (Figure 3.3 e), rGO nanosheets and PPyNTs are observed. The agglomeration of rGO is less in the ternary nanocomposite due to the presence of MoS_2 nanosheets on rGO (Figure 3.3 f).
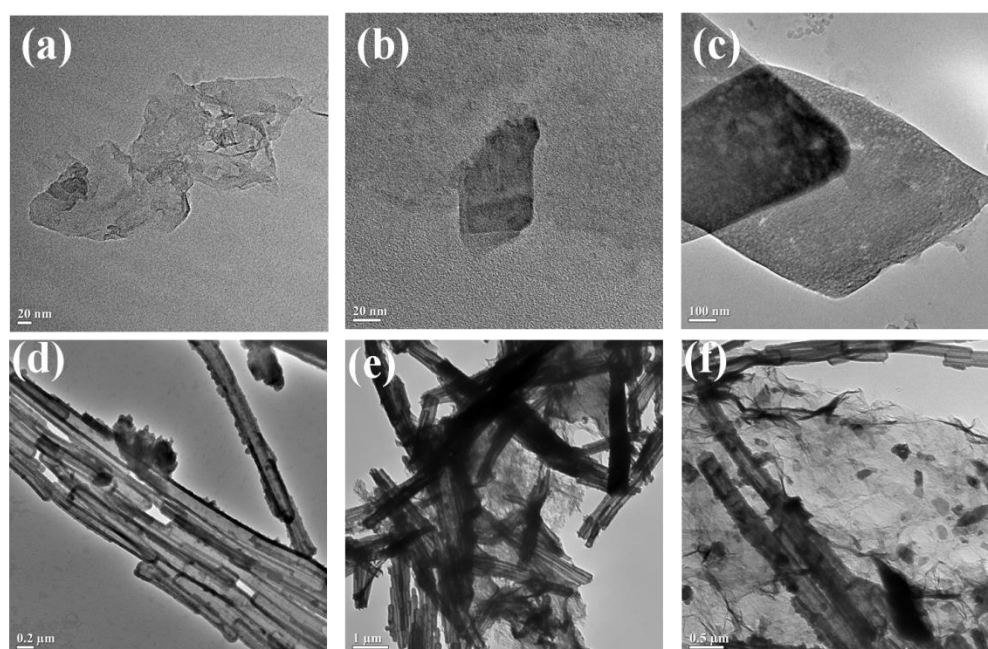
Figure 3.3: TEM Image of (a) MoS_2, (b) reduced graphene oxide (rGO), (c) MoS_2-rGO, (d) PPyNTs, (e) rGO-PPyNTs and (f) MoS_2-rGO/PPyNTs.

3.3.5 X-ray diffraction (XRD) analysis: X-ray diffraction analysis was conducted for bulk and exfoliated MoS_2 to understand the crystal structure (Figure 3.4). The XRD pattern of bulk MoS_2 exhibits an intense peak at $2\theta = 14.42^o$, corresponding to (002) plane with an inter-planner spacing of 0.614 nm. The other peaks of bulk MoS_2 are located at $2\theta = 29.02$, 32.74, 35.84, 39.52, 44.16, 49.86, 58.3 which are corresponding to (004), (100), (102), (103), (106), (105) and (110) planes respectively
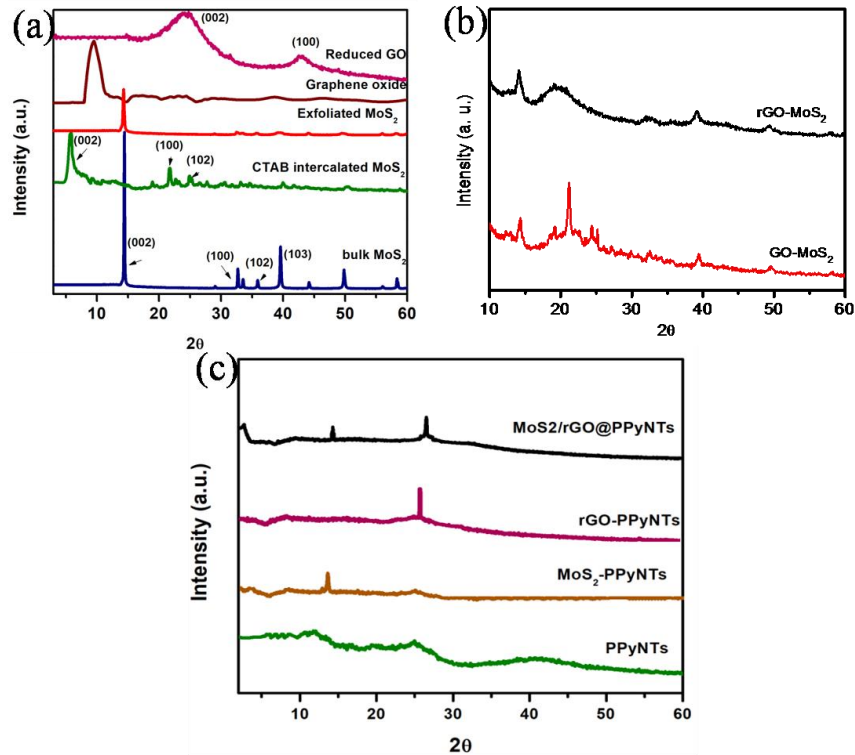
Figure 3.4: XRD spectra of (a) bulk MoS$_2$, intercalated MoS$_2$, Exfoliated MoS$_2$, GO and rGO, (b) MoS$_2$/GO and MoS$_2$/rGO, (c) PPyNTs, MoS$_2$-PPyNTs, rGO-PPyNTs, MoS$_2$-rGO/PPyNTs.

(JCPDS no. 77-1716). The peak corresponding to (002) plane is shifted to $2\theta = 5.74^o$ (inter-layer spacing 1.53 nm) after ultrasonication due to the insertion of long alkyl chain of CTAB [6]. The XRD peaks for exfoliated MoS$_2$ nanosheets are disappeared completely except a small peak at 14.42 ^{o} for (002). This peak develops due to random restacking of MoS$_2$ layers during drying process and the weak intensity indicates limited number of restacked layers [7]. Graphene oxide shows a diffraction peak at $2\theta = 9.45^o$ ((002) plane) possessing inter-planner spacing of 0.934 nm. This peak has shifted to $2\theta = 25.02^o$ after reduction of GO (d- spacing 0.356 nm). The small broad diffraction peak appeared at $2\theta = 42.97^o$ ((100) plane) indicates the short range restacking of graphene layers after reduction [8]. The diffraction pattern of MoS$_2$-rGO composite exhibits a new broad peak at $2\theta = 19.71^o$. The shifting of the peak could be due to the intercalation of MoS$_2$ nanosheets in GO. XRD spectrum of pure PPyNTs exhibits a broad amorphous characteristic polymer peak around $2\theta = 25.51^o$ attributed to the $\pi - \pi$ interaction of the polymer chains [9]. XRD of MoS$_2$-

PPyNTs nanocomposite displays both the characteristic peaks of MoS_2 and PPyNTs. The peak at $2\theta = 26^o$ in the XRD pattern of rGO-PPyNTs binary nanocomposites attributed to the overlapping of (002) plane of rGO with PPyNTs polymer peak. The diffraction pattern of MoS_2-rGO/PPyNTs shows a broad hump at $2\theta = 15^o - 35^o$, which may be due to the overlapping of MoS_2 intercalated rGO peak at $2\theta = 19.71^o$ and amorphous PPyNTs peak. A small broad peak is also observed at $2\theta = 14.42^o$.

3.3.6 Thermo-gravimetric (TGA) analysis: TGA measurement was performed under constant flow of nitrogen gas at a heating rate of 20 °/min for the four synthesized nanocomposites (Figure 3.5). The first slop is observed at around 100 °C for all four nanocomposites due to the evaporation of surface trapped moisture. For pure PPyNTs, weight loss at around 281 °C is attributed to the degradation of PPy [5]. Pure PPyNTs matrix exhibits total weight loss of 78% at 800 °C which has improved to 72.1% for the binary rGO-PPyNTs nanocomposites. The curvature of the TGA.
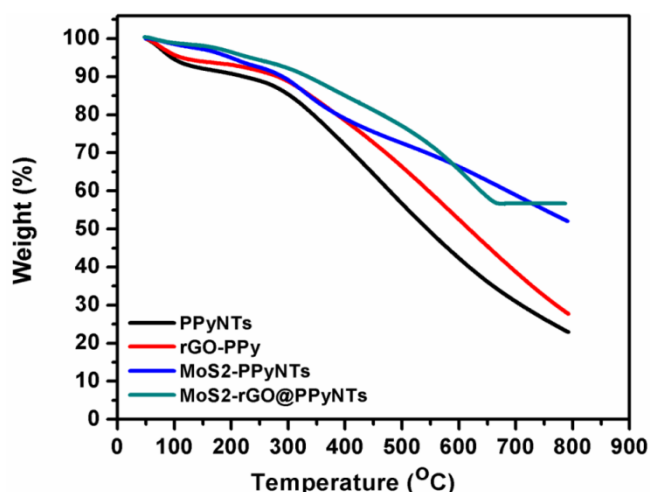

Figure 3.5: TGA thermographs of PPyNTs, rGO-PPyNTs, MoS_2-PPyNTs, MoS_2-rGO/PPyNTs.

curve in the range of 240-263 °C for MoS_2-PPyNTs and MoS_2-rGO/PPyNTs can be ascribed to the decomposition of CTAB chains present at the surface of MoS_2 [10]. The major weight loss at around 425-535 °C for MoS_2-PPyNTs and MoS_2-rGO/PPyNTs nanocomposites are observed due to the oxidation of MoS_2 to MoO_3 [11]. Continuous weight loss at 367-519 °C for MoS_2-rGO/PPyNTs nanocomposite is related to the degradation of graphene material present in the nanocomposite. The

ternary nanocomposite possesses highest thermal stability with a weight loss of only 43.31% at 800 °C

3.3.7 Brunauer–Emmett–Teller (BET) measurements: The adsorption-desorption isotherms of MoS$_2$-PPyNTs, rGO-PPyNTs and MoS$_2$-rGO/PPyNTs nanocomposites exhibit type IV characteristic, indicating the presence of large pores (Figure 3.6). BET specific area for rGO-PPyNTs and MoS$_2$-PPyNTs are 171.862 m^{2}g^{-1} and 469.014 m^{2}g^{-1}. Ternary MoS$_2$-rGO/PPyNTs nanocomposite is considered to be the best one with specific surface area of 625.456 m^{2}g^{-1}. The higher specific area of ternary nanocomposites is attributed to the MoS$_2$-rGO layer-by-layer structures as MoS$_2$ prevent the agglomeration of rGO nanosheets which is expected to beneficial for electrochemical charge storage. Pore size distribution is calculated from BJH method. The average pore size for the ternary nanocomposites is 6.85 nm.
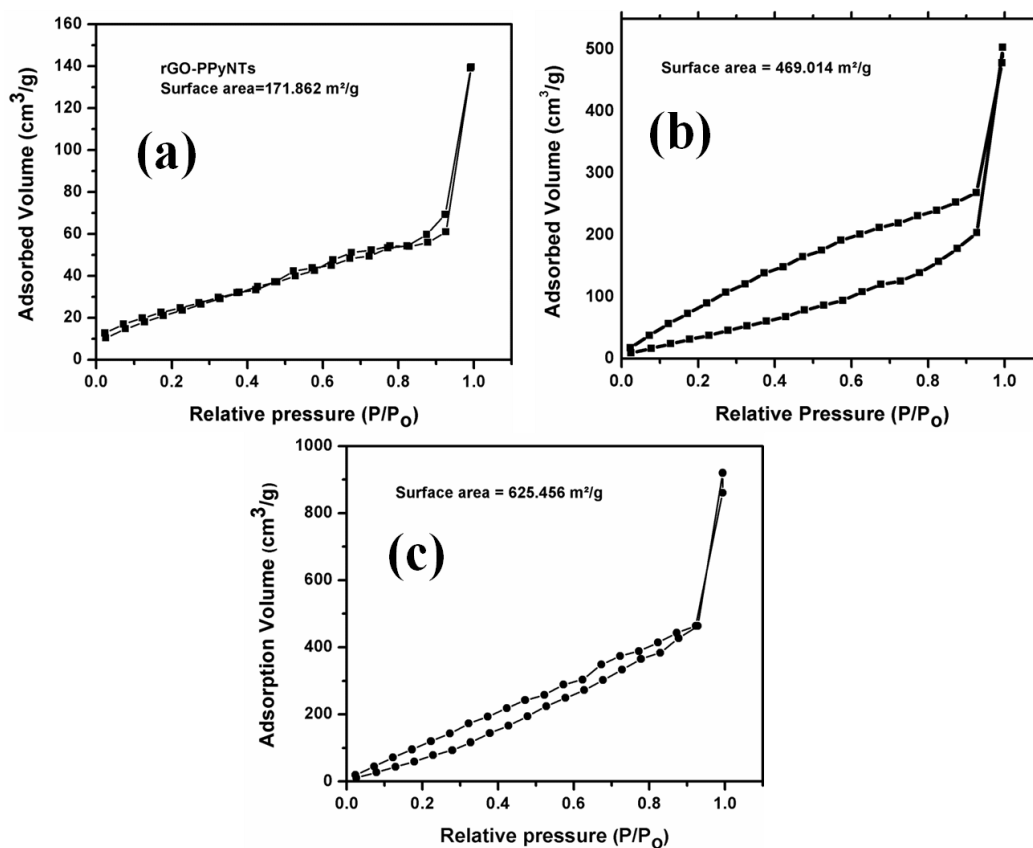

Figure 3.6: Nitrogen adsorption-desorption isotherms of (a) rGO-PPyNTs, (b) MoS$_2$-PPyNTs and (c) MoS$_2$-rGO/PPyNTs.

3.4 Electrochemical characterization

Electrochemical properties of the ternary MoS_2-rGO/PPyNTs nanocomposite and the other synthesized electrodes i.e. PPyNTs, rGO-PPyNTs, MoS_2-PPyNTs were studied with cyclic voltammetry (CV) and galvanostatic charge-discharge (GCD) at a potential window of -0.2 V to 0.6 V (vs. Ag/AgCl) in 1 M KCl electrolyte.

3.4.1 Electrochemical measurement of the electrodes: Cyclic voltammograms of the four electrodes are shown in the Figure 3.7 (a) at the scan rate of 20 mVs^{-1} in 1 M KCl electrolyte. KCl is the widely used electrolyte for electrochemical supercapacitors due to its larger electrochemical window along with less corrosion towards the electrode material and batter safety [12]. Pure PPyNTs electrode exhibits nonrectangular behaviour in CV measurements indicating the pseudocapacitive nature [13]. The CV curve possesses rectangular geometry after incorporation of rGO into the polymer matrix, indicates of EDL capacitance (Figure 3.7 a). MoS_2-PPyNTs
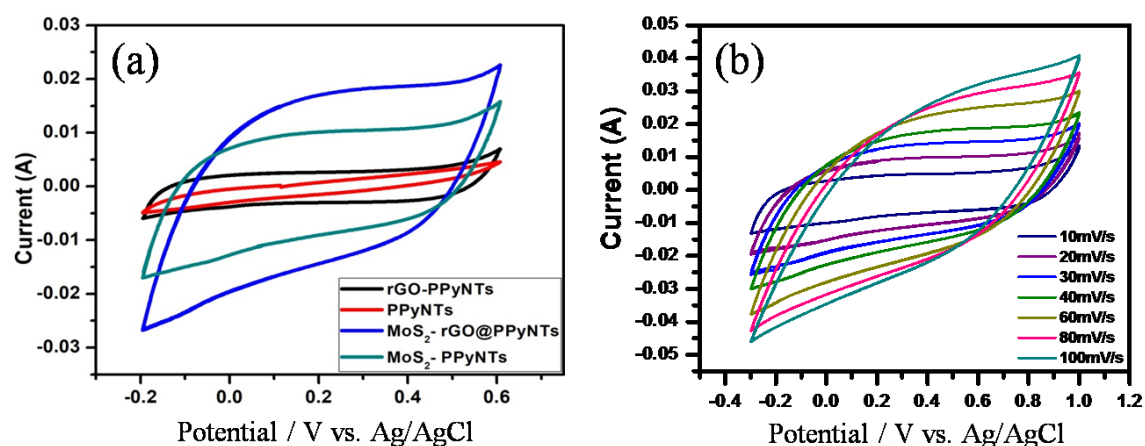
Figure 3.7: CV curve of PPyNTs, rGO-PPyNTs, MoS_2-PPyNTs and MoS_2-rGO/PPyNTs at a scan rate of 20 mVs^{-1} and (b) CV of MoS_2-rGO/PPyNTs at various scan rates ranging from 10-100 mVs^{-1}.

electrode exhibits larger area under the CV curve as compare to rGO-PPyNTs, suggesting improvement in capacitive behaviour upon incorporation of MoS_2 in the polymer matrix. MoS_2 effectively prevents the agglomeration of polymer matrix within the binary nanocomposite, leading to greater surface area. A slight redox peak appears as a result of faradic reactions for MoS_2-PPyNTs nanocomposite. At the same time, rectangular CV pattern of MoS_2-PPyNTs indicates the presence of EDLC mechanism also. Therefore both EDLC and pseudocapacitance charge storage

mechanisms are present in MoS$_2$/PPyNTs binary nanocomposites. MoS$_2$-rGO/PPyNTs ternary electrode possesses the highest capacitive response. This could be due to the minimum agglomeration of rGO nanosheets in the MoS$_2$-rGO structures [14]. Figure 3.7 (b) shows the CV curves of the ternary nanocomposite at different scan rates of 10-100 mVs^{-1}. It is observed that with increasing scan rates, the current-voltage response also increases but specific capacitance decreases. It can be explained like- electrolyte ions is only permitted to the outer active surface area of the active material.

Figure 3.8 shows the galvanostatic charge-discharge measurement for PPyNTs, rGO-PPyNTs, MoS$_2$-PPyNTs and MoS$_2$-rGO/PPyNTs electrodes at a current density of 1 Ag^{-1} in the potential window of -0.2 V to 0.6 V (vs. Ag/AgCl). Current is supplied to the working electrode against the reference electrode and the resulting potentials were measured as a function of time. Specific capacitance (C_{sp}) is calculated using the following equation (3.1) and coulombic efficiency (η) from the equation (3.2):

$$C_{sp} = \frac{I \times \Delta T_d}{m \times \Delta V} \qquad (3.1)$$

$$\eta = \frac{\Delta T_d}{\Delta T_c} \times 100 \qquad (3.2)$$

where $I, \Delta T_d, \Delta T_c, m, \Delta V$ stand for constant discharge current, discharge period, charging time, mass of the active material loaded in the electrode and potential drop during discharge process. The GCD curve of PPyNTs electrode is slightly deviating from linearity due to the fast reversible redox processes [13]. The non-linear shape of rGO-PPyNTs electrode may be due to the dominating pseudocapacitance from PPyNTs. A triangle shaped GCD curve is observed for MoS$_2$-PPyNTs electrode suggesting that the maximum contribution from EDLC storage process as voltage changes linearly as a function of time. The ternary MoS$_2$-rGO/PPyNTs electrode possesses highest gravimetric discharge period and maximum specific capacitance. The first two part of the discharge curve is perfectly linear with two slopes which suggests ELDC behavior. The later parts of the GCD curve of the ternary electrode is nonlinear and could be due to pseudocapacitance. The calculated specific capacitances for PPyNTs, rGO-PPyNTs, MoS$_2$-PPyNTs and MoS$_2$-rGO/PPyNTs nanocomposites are 313.75 Fg^{-1}, 625 Fg^{-1}, 1249.36 Fg^{-1} and 1561.25 Fg^{-1} respectively
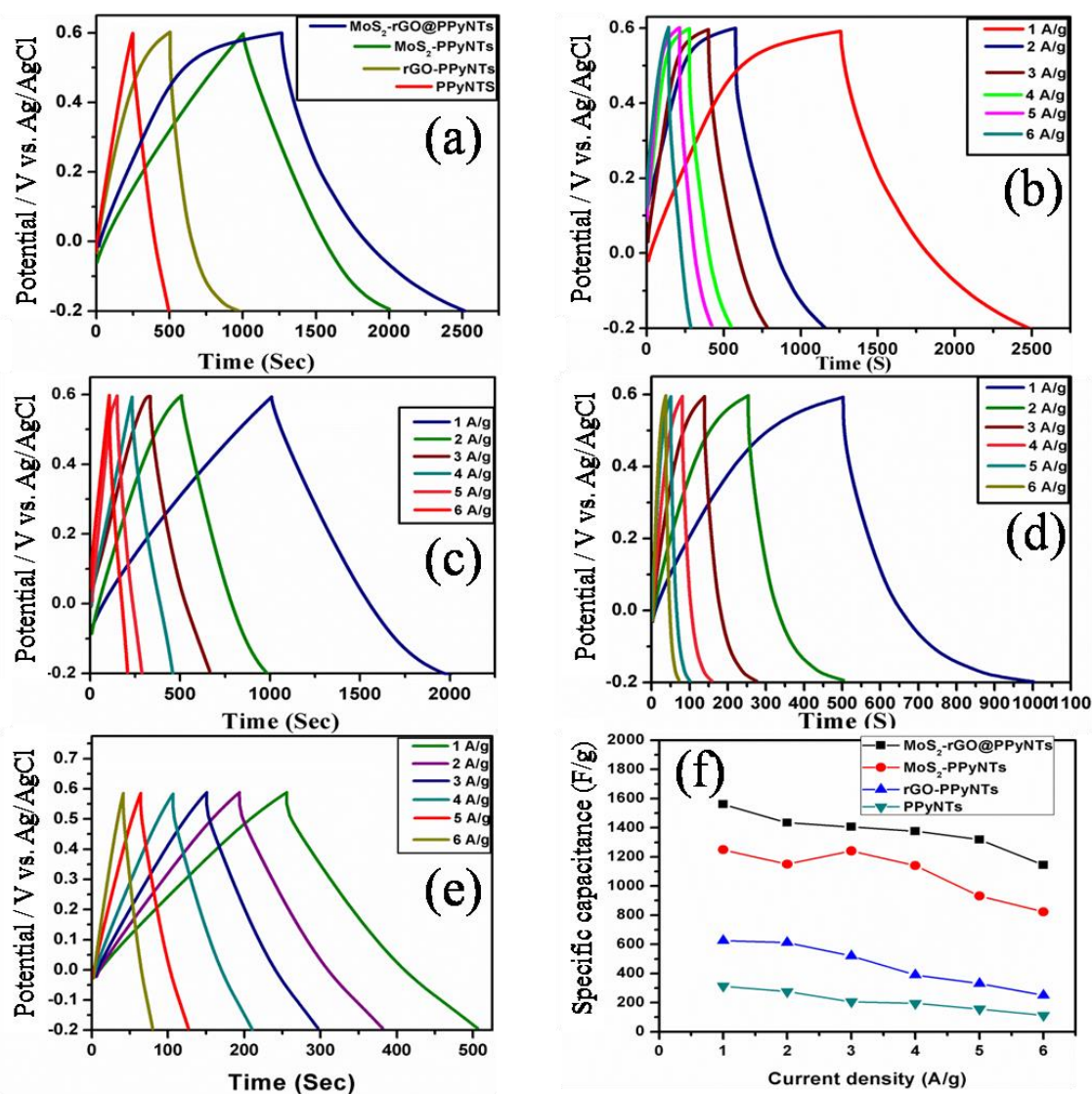
Figure 3.8: GCD curve of (a) PPyNTs, rGO-PPyNTs, MoS$_2$/PPyNTs and MoS$_2$-rGO/PPyNTs at current density 1 Ag^{-1}, (b) shows the GCD of MoS$_2$-rGO/PPyNTs at current densities from (1-6) Ag^{-1}, (c) MoS$_2$-PPyNTs ,(d) rGO-PPyNTs and (e) PPyNTs at current density range (1-6) Ag^{-1}, and (f) specific capacitance vs. current density plot.

at the current density of 1 Ag^{-1}. The reasons for maximum specific capacitance of the ternary electrode are: (i) pseudocapacitance contribution from Polypyrrole nanotubes, (ii) more number of interfaces, minimum agglomeration in the nanosheets and electro-active sites from the MoS$_2$-rGO layer-by-layer structures and (iii) high specific surface area of MoS$_2$-rGO/PPyNTs (BET measurement). Figure 3.8 (b-e) shows the gravimetric charge-discharge curves for MoS$_2$-rGO/PPyNTs, MoS$_2$-PPyNTS, rGO-PPyNTs and PPyNTs at the current densities of 1-6 Ag^{-1}. It is observed that the

discharge duration decreases with increasing current densities so as the specific capacitance which may be attributed to the participation of outer layers only in the charging-discharging processes. The specific capacitances of the four synthesized electrodes with various current densities are shown in Figure 3.8 (f). The specific capacitance of PPyNTs, rGO-PPyNTs, MoS$_2$-PPyNTs and MoS$_2$-rGO/PPyNTs electrodes are calculated to be 112.5 Fg^{-1}, 251.25 Fg^{-1}, 823.7 Fg^{-1} and 1145.2 Fg^{-1} at current densities of 6 Ag^{-1} which are 35.86%, 40.2%, 65.92%, 73.35%, respectively of the initial capacitance at 1 Ag^{-1} of current density. It suggests a good rate capability of the ternary nanocomposites. Internal resistance (IR) drop is an important parameter for supercapacitor electrodes as the higher value of which can develop over-potential at the electrode surface leading to the consumption of electrolyte ions at the electrode surface. Almost 100% Coulombic efficiency of the ternary nanocomposites has strongly suggested the presence of efficient storage processes and elevated electrochemical reversibility of the electrode.
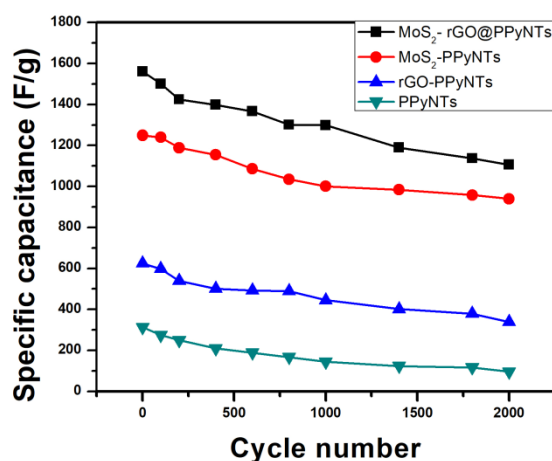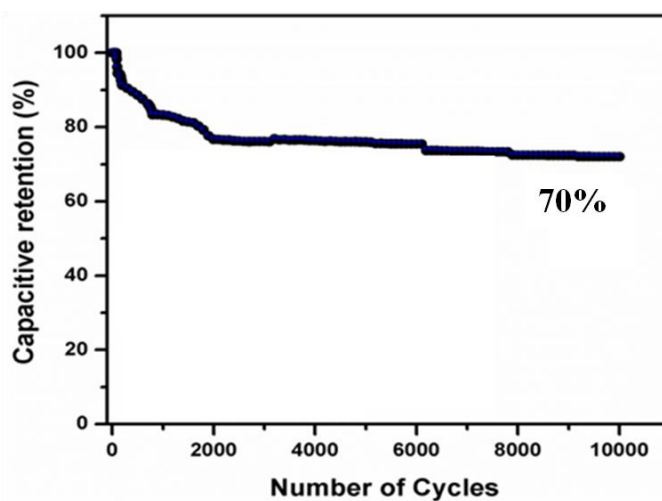

Figure 3.9: Cycling stability with cycle numbers for the PPyNTs, rGO-PPyNTs, MoS$_2$/PPy and MoS$_2$-rGO/PPyNTs nanocomposites.

Cycling stability is an important parameter of supercapacitor electrodes for its potential application in power supply. Pseudocapacitive materials with very high energy density sacrifice cycle life whereas EDLC source possesses extremely impressive cycle life. Cyclic stability of the four synthesized electrodes were evaluated with galvanostatic charge/discharge measurements at 1 Ag^{-1} of current density and the specific capacitances with cycle numbers are shown in Figure 3.9. PPyNTs and rGO-PPyNTs possessed 30.5% and 54.24% of specific capacitance

retention at 2000 cycles whereas MoS_2-PPyNTs possessed 75.2% of retention of the initial specific capacitance. Ternary MoS_2-rGO/PPyNTs electrode exhibited 76.68% of capacitive retention. Polypyrrole nanotubes exhibited poor cycle life due to volume instability in cycling process. Interestingly, incorporation of rGO in the polymer matrix shows distinct enhancement in cycling performance of the binary rGO-PPyNTs electrode. Highest cycling stability was observed for the MoS_2-rGO/PPyNTs ternary nanocomposites.

For the better understanding of cycling stability of MoS_2-rGO/PPyNTs ternary electrode, GCD was evaluated at a current density of 10 Ag^{-1} for 10,000 cycles. The graph of the capacitive retention (%) vs. cycle numbers is displayed in Figure 3.10. The specific capacitance of the ternary electrode remains constant up to the 82 repeated cycles. 83.21% stability is observed after 1000 GCD cycles. Capacitive retention of 75.48% is obtained after 2000 for the ternary electrode. Finally, the ternary nanocomposite exhibits 72% of cycling stability after 10,000 GCD cycles (Figure 3.10).

Figure 3.10: Cycling stability of MoS_2-rGO/PPyNTs electrode with cycle numbers at the current density of 10 Ag^{-1} for 10,000 repeated GCD cycles.

Ex-situ scanning electron microscope (SEM) of the fresh and cycled electrodes were taken and are shown in Figure 3.11. SEM micrographs were taken at two different magnifications for the fresh electrodes (Figure 3.11 a, b). It is observed that the PPyNTs have completely covered the MoS_2-rGO layered structures in the fresh electrodes. Pseudocapacitive materials possess low cycling stability due to the

swelling and shrinkage during cycling process. This may cause mechanical degradation in the electrode material, as a result of which capacitive performances of the electrode degrades. It is observed that PPyNTs covering has been removed from some parts of the electrode's surface and sheet like morphology can be seen in the SEM images (Figure 3.11 c, d) after 10,000 GCD cycles. These changes may be attributed to the swelling and shrinkage in the PPyNTs during GCD cycling. Due to the shrinkage of the PPyNTs, large holes and degradation of the nanotubes are also observed from the SEM micrographs (Figure 3.11 d), which may reduce the interface area between the PPyNTs and MoS_2-rGO layer-by-layer structure on the electrode surface and as a result specific capacitance decreases.
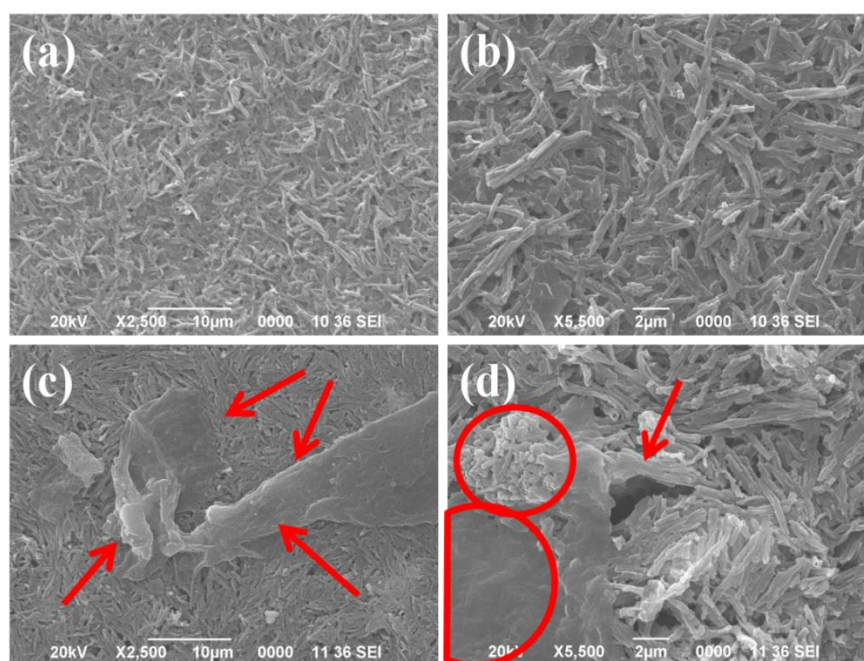
Figure 3.11: SEM micrographs of (a) and (b) MoS_2-rGO/PPyNTs/ITO electrode before cycling at two different magnifications and (c) and (d) MoS_2-rGO/PPyNTs/ITO electrode after cycling at two different magnifications.

EIS was carried for the better understanding of electrode kinetics and performed for the frequency range of 10 µHz-10^5 Hz (Figure 3.12). Nyquist plots of MoS_2-rGO/PPyNTs, MoS_2-PPyNTs, rGO-PPyNTs and PPyNTs show a straight line towards the lower frequency side and a quasi semicircular arc at the high frequency region. The intercept of the high frequency loop at X-axis defines equivalent series resistance (R_s) which is the measure of intrinsic resistance of the electrode and

electrolyte's ionic resistance whereas the diameter of the arc represents the charge transfer resistance (R_{ct}). Nyquist plot implies that the R_s (2.59 Ω) of rGO-PPyNTs electrode is much smaller then PPyNTS electrode (7.01 Ω) which may be due to the incorporation of conductive rGO nanosheets. The R_s for MoS$_2$-PPyNTs and MoS$_2$-rGO/PPyNTs is calculated to be 1.75 Ω and 1.09 Ω respectively. Smaller value of R_s is due to the lower intrinsic resistance of the electrode. 27 Ω, 11 Ω, 4.13 Ω and 5.4 Ω are the obtained values of R_{ct} from Nyquist plot corresponding to PPyNTS, rGO-PPyNTs, MoS$_2$-PPyNTs and MoS$_2$-rGO/PPyNTs respectively. It has been observed that the charge transfer resistance of PPyNTs decreases when highly conductive rGO is incorporated and further reduces by MoS$_2$ as it can alleviate the agglomeration of PPyNTs, suggesting an efficient charge transport process. It is interesting to note that, charge transfer resistance is slightly higher for the ternary one as compared to MoS$_2$-PPyNTs, which may be due to the presence of three components within the same surface area of the electrode, arrests the charge flow to some level at the electrode-electrolyte interfaces [14]. Towards the low frequency region, a vertical line almost parallel to the imaginary axis (Y-axis) of the complex plot has been observed and the slop corresponding to the MoS$_2$-rGO/PPyNTs nanocomposite is near about 1.
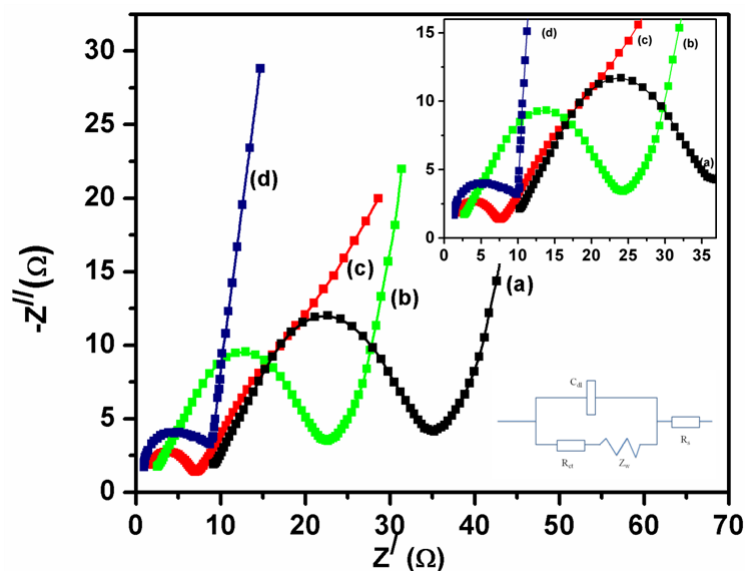
Figure 3.12: Nyquist plots for (a) PPyNTs, (b) rGO-PPyNTs, (c) MoS$_2$-PPyNTs, (d) MoS$_2$-rGO/PPyNTs.

3.4.2 Electrochemical measurements of symmetric supercapacitor: The electrochemical performances for PPyNTs, rGO-PPyNTs, MoS$_2$-PPyNTs and MoS$_2$-

rGO/PPyNTs electrodes have been discussed so far. Ternary MoS$_2$-rGO/PPyNTs electrode has shown maximum electrochemical performance compared to the binary electrodes and hence selected to evaluate the electrode performances in two electrode symmetric cell set-up. Symmetric supercapacitor (SSC) set-up was arranged by using MoS$_2$-rGO/PPyNTs electrode both in positive and negative terminals. Electrochemical performances of the symmetric supercapacitor were investigated in 1 M KCl aqueous electrolyte. The optimized potential window for the MoS$_2$-rGO/PPyNTs // MoS$_2$-rGO/PPyNTs symmetric supercapacitor was investigated from a set of CV measurements at scan rate of 10 mVs^{-1} (Figure 3.13 a) by increasing potential from 0 V to 1.5 V. The potential window of the symmetric supercapacitor
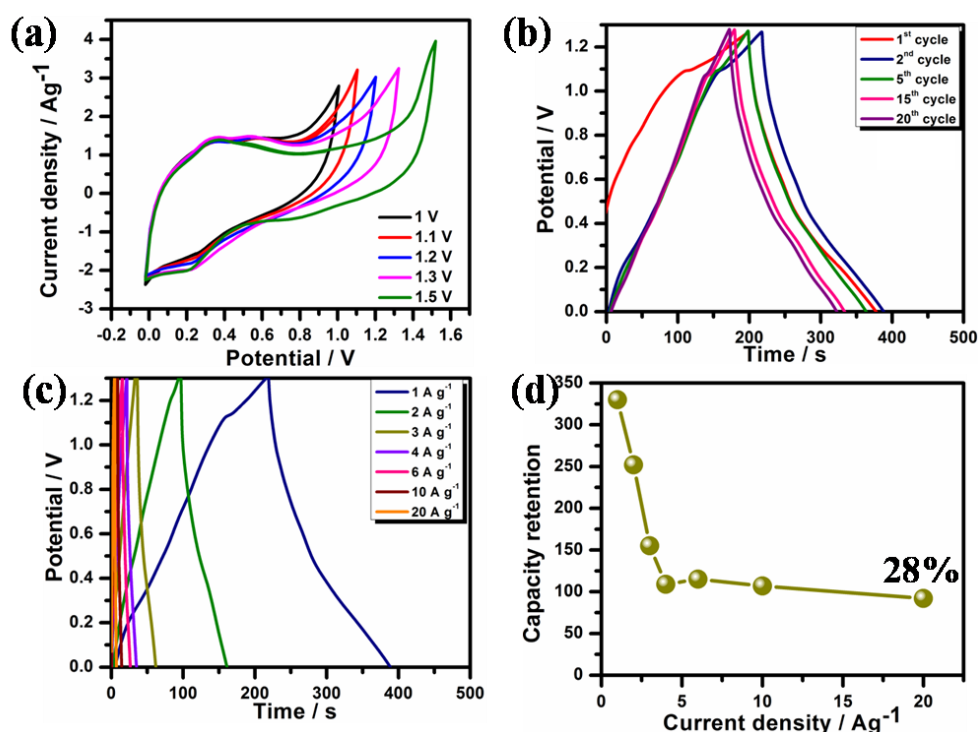

Figure 3.13: CV for potential window optimization (a), (b) GCD at 1 Ag^{-1} current density for first 20th cycles, (d) GCD at different current densities, and (e) rate capability plot of MoS$_2$-rGO/PPyNTs // MoS$_2$-rGO/PPyNTs symmetric supercapacitor.

can be extended as high as 1.3 V beyond (Figure 3.13 a). Galvanostatic charge/discharge measurements were evaluated at the current densities of 1-20 Ag^{-1} in the optimized potential range (Figure 3.13 b, c). The non-linear GCD pattern suggests the presence of both EDLC and pseudocapacitance charge storage processes. Figure

3.13 b show the GCD curves of the symmetric supercapacitor at 1 Ag^{-1} of current density for the first 20th cycles. The rate capability plot for the fabricated symmetric supercapacitor is depicted in Figure 3.13 d. Specific capacitance for the symmetric supercapacitor was calculated to be 330 Fg^{-1} at 1 Ag^{-1} of current density and 92 Fg^{-1} at 20 Ag^{-1} possessing 27.8% of rate capability. It is obvious that at high current density (20 Ag^{-1}), charging/discharging processes are very quick.

Cycling stability of the MoS$_2$-rGO/PPyNTs // MoS$_2$-rGO/PPyNTs symmetric supercapacitor has been evaluated for 5000 repeated GCD cycles at the current density of 20 Ag^{-1}. The specific capacitance retention vs. cycle numbers plot is shown in Figure 3.14 a. The MoS$_2$-rGO/PPyNTs // MoS$_2$-rGO/PPyNTs symmetric supercapacitor exhibits specific capacitance of 92 Fg^{-1} for the first cycle, 52.3 Fg^{-1} for the 1000 cycle and 49 Fg^{-1} for the 5000 cycles. The symmetric supercapacitor possesses only 53.2% of cycling stability after 5000 repeated GCD cycles.
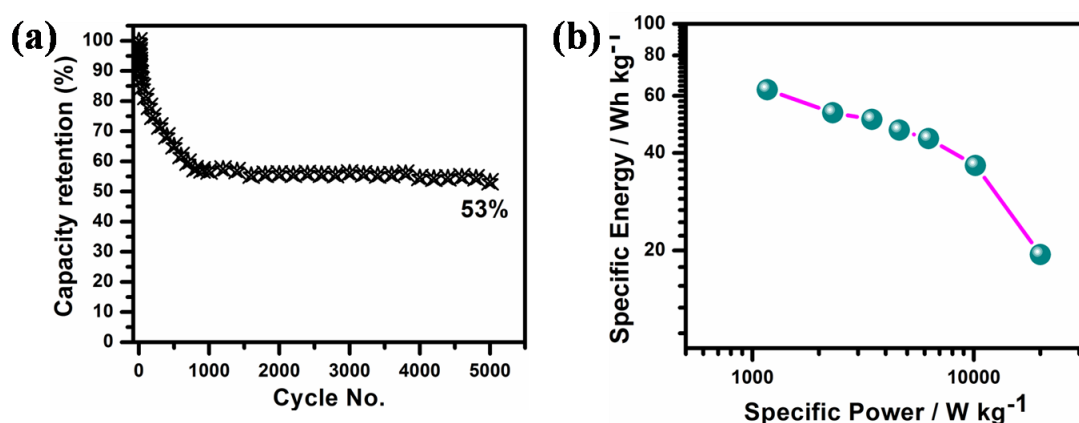
Figure 3.14: Cycling stability plot of MoS$_2$-rGO/PPyNTs // MoS$_2$-rGO/PPyNTs symmetric supercapacitor for 5000 cycles, and (b) Ragone plot of MoS$_2$-rGO/PPyNTs // MoS$_2$-rGO/PPyNTs symmetric supercapacitor.

The specific energy and specific power of MoS$_2$-rGO/PPyNTs // MoS$_2$-rGO/PPyNTs symmetric supercapacitor were calculated from GCD measurements for the range of current densities from 1 to 20 Ag^{-1}. These calculated values of specific power and energy are shown as Ragone plot in Figure 3.14 b. MoS$_2$-rGO/PPyNTs // MoS$_2$-rGO/PPyNTs symmetric supercapacitor delivers specific energy of 62.7 Whkg^{-1} for specific power of 1167 Wkg^{-1} at 1 Ag^{-1} of current density.

3.5 Conclusion

Layer-by-layer structure of MoS$_2$-GO was synthesized from the oppositely charged nanosheets. Ternary nanocomposite of MoS$_2$-rGO/PPyNTs was prepared by adding 40 wt% of PPyNTs, followed by hydrothermal reduction of GOs. Zeta potential measurement indicates the presence of oppositely charged surface charges on MoS$_2$ (positively charges) and GO (negatively charged) nanosheets. SEM micrograph discloses the presence of porous heterogeneous layer-by-layer structures of MoS$_2$-GO. XRD patterns reveal the successful exfoliation of bulk MoS$_2$ in presence of CTAB and the shifting of the diffraction peaks towards lower diffraction angles confirms the formation of MoS$_2$-rGO layer-by-layer structures. This structure prevents agglomeration of rGO nanosheets and restacking of MoS$_2$ nanosheets. MoS$_2$-rGO/PPyNTs ternary electrode delivers high specific capacitance of 1561.25 Fg^{-1} at 1 Ag^{-1} current density and specific capacitance of 1145.2 Fg^{-1} at 6 Ag^{-1} exhibiting an excellent rate performance. MoS$_2$-rGO/PPyNTs ternary electrode exhibits 72% of cycling stability after 10,000 galvanostatic charge/discharge cycles at 10 Ag^{-1} of current density. MoS$_2$-rGO/PPyNTs // MoS$_2$-rGO/PPyNTs symmetric supercapacitor delivers specific capacitance of 330 Fg^{-1} at 1 Ag^{-1} of current density and rate capability of 28% at 20 Ag^{-1}. The supercapacitor exhibits cycling stability of 53% after 5000 charge/discharge cycle at 20 Ag^{-1} of current density. Moreover, specific energy of 62.7 Whkg^{-1} could be estimated with a specific power of 1167 Wkg^{-1} based on the total mass at 1 Ag^{-1} of current density.

3.6 References

[1] Ko, J. M., Rhee, H. W., Park, S.M., and Kim, C. Y. Morphology and Electrochemical Properties of Polypyrrole Films Prepared in Aqueous and Nonaqueous Solvents. *Journal of the Electrochemical Society*, 137(3): 905-909, 1990.

[2] Zhao, J., Wu, J., Li, B., Du, W., Huang, Q., Zheng, M., Xue, H., and Pang, H. Facile synthesis of polypyrrole nanowires for high-performance supercapacitor electrode materials. *Progress in Natural Science: Materials International*, 26: 237–242, 2016.

[3] Santino, L.M., Hwang, E., Diao, Y., Lu, Y., Wang, H., Jiang, Q., Singamaneni, S., and D'Arcy, J.M. Condensing vapor phase polymerization (cvpp) of

electrochemically capacitive and stable polypyrrole microtubes. *ACS applied materials & interfaces*, 9(47):.41496-41504, 2017.

[4] Yu, H., Zhang, B., Bulin, C., Li, R., and Xing, R. High-efficient synthesis of graphene oxide based on improved hummers method. *Scientific reports*, 6: 36143, 2016.

[5] Upadhyay, J., and Kumar, A. Structural, thermal and dielectric studies of polypyrrole nanotubes synthesized by reactive self degrade template method. *Materials Science and Engineering: B*, 178(15): 982-989, 2013.

[6] Zheng, J., Zhang, H., Dong, S., Liu, Y., Tai Nai, C., Suk Shin, H., Young Jeong, H., Liu, B., and Ping Loh, K. High yield exfoliation of two-dimensional chalcogenides using sodium naphthalenide. *Nature communications*, 5(1): 1-7, 2014.

[7] Ji, S., Yang, Z., Zhang, C., Liu, Z., Tjiu, W. W., Phang, I. Y., Zhang, Z., Pan, J., and Liu, T. Exfoliated MoS2 nanosheets as efficient catalysts for electrochemical hydrogen evolution. *Electrochimica Acta* 109: 269-275, 2013.

[8] Stobinski, L., Lesiaka, B., Malolepszy, A., Mazurkiewicz, M., Mierzwa, B., Zemek, J., Jiricek, P., and Bieloshapka, I. Graphene oxide and reduced graphene oxide studied by the XRD, TEM and electron spectroscopy methods. *Journal of Electron Spectroscopy and Related Phenomena*, 195: 145–154, 2014.

[9] Chitte, H.K., Shinde, G.N., Bhat, N.V., and Walunj, V.E. Synthesis of polypyrrole using ferric chloride (FeCl$_3$) as oxidant together with some dopants for use in gas sensors. *Journal of sensor technology*, 1(2): 47, 2011.

[10] Liu, L., Huang, Z., and Huang, P. Fabrication of coral-like MoS2 and its application in improving the tribological performance of liquid paraffin. *Tribology International*, 104: 303-308, 2016.

[11] Wang, Z., Chen, T., Chen, W., Chang, K., Ma, L., Huang, G., Chen, D., and Lee, J.Y. CTAB-assisted synthesis of single-layer MoS2–graphene composites as anode materials of Li-ion batteries. *Journal of Materials Chemistry A*, 1(6): 2202-2210, 2013.

[12] Zhong, C., Deng, Y., Hu, W., Qiao, J., Zhang, L., and Zhang, J. A review of electrolyte materials and compositions for electrochemical supercapacitors. *Chemical Society Reviews*, 44(21): 7484-7539, 2015.

[13] Devi, M., and Kumar, A. In-situ reduced graphene oxide nanosheets-polypyrrole nanotubes nanocomposites for supercapacitor applications. *Synthetic Materials,* 222: 318-329, 2016.

[14] Huang, K.J., Wang, L., Liu, Y.J., Wang, H.B., Liu, Y.M., and Wang, L.L. Synthesis of polyaniline/2-dimensional graphene analog MoS_2 composites for high-performance supercapacitor. *Electrochimica Acta*, 109: 587-594, 2013.